

Final Report: Applying Machine Learning Models on Detecting and Predicting Coastal Upwelling in Arabian Sea Region

Jiarui Yu and Minh Phan

Summer 2023

Abstract

In this internship report, we investigate the phenomenon of coastal upwelling in specific global regions and its significant economic implications on the local fisheries industry. Utilizing diverse climate variables obtained from governmental remote sensing data sources worldwide, we integrated this data into a cohesive dataset. We employed advanced unsupervised and supervised machine learning techniques to identify coastal upwelling zones in the Arabian Sea region and forecast sea surface temperatures. Our research involved a comparative analysis of prediction efficiency using Transformer, ConvLSTM, and their combination. Remarkably, ConvLSTM outperformed other models by a considerable margin. Additionally, we conducted a detailed evaluation of EfficientNet and U-Net segmentation models, exploring their potential in the detection analysis.

1 Introduction

Upwelling is a phenomenon by which subsurface water from the deep parts of the ocean reaches the surface and alters the physical and chemical properties of water, including salinity and temperature (Lahiri and Vissa, 2022; Vinayachandran et al., 2002). The convective mixing effect from upwelling brought nutrients to the surface, which at the same time increase marine production, and eventually primary productivity which the fisheries are dependent on (Cushing, 1971). Given its substantial economic impact, the need of detection and prediction models on this phenomenon naturally ensues. State-of-the-art technologies, including machine learning algorithms, used in detecting upwelling is not something new, but are quite still limited (Hammond et al., 2022; Jebri et al., 2022; Picado et al., 2023). This paper serves to provide more examples and architecture we can explore with to expand our understanding on the natural phenomenon, especially predicting its occurrence and narrow down their primary zones, beginning with the key variable: sea surface temperature.

2 Background

Sea Surface Temperature (SST) has long been recognized as a critical parameter in the study of marine and atmospheric systems. As a key factor driving the heat exchange between the ocean and atmosphere, SST plays an instrumental role in influencing regional weather patterns, climate variability, and even the distribution of marine ecosystems. Understanding anomalies like upwelling events, where colder deep waters replace warmer surface waters, is crucial not just for marine biologists and fishery management, but also for improving our global climate models (Reynolds et al., 2002).

Traditionally, the detection and analysis of such marine phenomena relied on satellite imaging, buoy data, and occasionally ship-borne measurements. However, with the surging tide of technological advancements, the application of deep learning in the oceanographic realm has gained momentum. Recognizing the need for high-quality, comprehensive data to drive these advancements, we’ve created a Zarr database, compiling an array of marine parameters, from SST to wind speed. By processing vast amounts of SST data images from this database, neural networks promise a promising level of precision and granularity in detecting marine events. Yet, these tools are not without their challenges. The black-box nature of deep learning models often necessitates supplementary tools like LIME to interpret their results.

SST is one of many variables whose data can be collected using remote sensing (NASA/JPL, 2015). Remote sensing data refers to any data that are acquired at a distance using reflected radiation from a surface, and analyzing this reflection data can unveil lots of information about the said surface (Senf, 2022). Therefore, analyzing remote sensing data accumulated over time can help us explore the trends and changes of the ecosystems, and in our case, coastal upwelling trends.

In this study, we meld remote sensing data with state-of-the-art deep learning architectures. Our region of interest is specifically focused within a bounding box delineated by latitudes -5 degrees South to 32 degrees North and longitudes 42 to 120 degrees West. This region was chosen due to its significant marine activity and prevalent upwelling events, making it a hotspot for our analysis. From the sensitivity analyses of Transformer and ConvLSTM models to the detailed performance evaluation of the U-Net model, we aspire to not only detect upwelling events with enhanced precision but also contribute to the larger dialogue on marine research methodology. By bridging the gap between computational innovation and the vast expanse of our oceans, we seek to further our understanding of the intricacies of marine phenomena and their broader implications.

3 Data

To prepare the data for training the machine learning models, we developed a dataset incorporating various environmental variable indicators that are theoretically or scientifically proven to be correlated to the state of coastal upwelling, not limited to the region of interest.

3.1 Data sources

Most of our remote sensing data are sourced from the Copernicus program. Copernicus program is an European flagship program providing reliable and open satellite-based imagery, models, and in situ (nonspace) data, and is a coordinated effort between many organizations, including the European Commission, the European Space Agency, the European Centre for Medium-Range Weather Forecasts (ECMWF), and European Union Agencies (Skoda & Adam, 2020). Furthermore, we also blended data from the National Aeronautics and Space Administration (NASA) EarthData and the National Centers for Environmental Information (NCEI)’s databases. Listed below are the data sources that we collected from the Copernicus Data Store, the program’s official data access portal:

3.1.1 ERA5

The primary data source we used in this assembled dataset product is the Copernicus ERA5 Global Reanalysis, the fifth generation of an atmospheric reanalysis project from Copernicus and ECMWF (Hersbach et al., 2020). As an ongoing project, once completed, it will embody a “detailed record of the global atmosphere, land surface, and ocean waves from 1950 onwards” (Hersbach et al., 2020). However, only 1979 data onwards is currently publicly available for download. The dataset’s high temporal and spatial resolution and ranges are highly conceivable as it enables consistent, detailed, and concise detection and prediction tasks in our project. Comparing its performance to another popular reanalysis product, MERRA-2 by NASA, it overpowers the other in all aspects: resolution, time coverage, and accuracy (Olauson, 2018). Given its powerful capabilities, We collected five variables from this source, namely sea surface temperature, two-meter-high from surface level atmospheric temperature, and horizontal and vertical surface wind velocities. All of them are currently accessible using Amazon Simple Storage Service (S3) and updated regularly (Hersbach et al., 2020).

Sea surface temperature The temperature of the ocean’s surface, known as Sea Surface Temperature (SST), serves as a crucial gauge for assessing the Earth’s climate system (Reynolds et al., 2002). Consequently, having precise information about SST is vital for monitoring, researching, and forecasting climate patterns. This also rings true in the case of coastal upwelling, as seasonally variable low SST compared to the average temperature at the same latitude may partially indicate an upwelling zone (Benazzouz et al., 2014; Alvarez et al., 2010; Izumo et al., 2008).

Atmospheric temperature Our choice to include atmospheric temperature was more or less a secondary addition. It does not have a instant, direct correlation on upwelling as SST; however, researches showed that its strength may be influenced by preceding air temperature records in the preceding seasons before the upwelling season (Sun et al., 2022). This complements our project, especially on prediction tasks.

Vertical and horizontal components of the surface wind One of the prominent coastal upwelling characteristics is a parallel wind direction along the coast (Lill, 1978). Strong winds can also cool the ocean surface, promoting the conditions and occurrence of upwelling (Kim et al., 2023). Longshore surface wind is also a major factor in mass transport and upwelling intensity, especially in the case of wind stress (Nigam et al., 2018). In their paper, Nigam et al. (2018) mentioned a formula, $\tau_y = \rho_d |W| v$, addressing the relationship between the meridional wind stress (τ_y), wind speed (W), and v (meridional wind component, or more informally known as the vertical component of the wind).

3.1.2 Global Ocean Physics Reanalysis

The Global Ocean Physics Reanalysis (product code name GLORYS12V1) is the first version of a Copernicus Marine Environment Monitoring Service (CMEMS)’s reanalysis product covering an 5000m elevation range from 1993, with models used for reanalysis similar to ERA5’s (European Union-Copernicus Marine Service, 2018). It covers a wide range of variables such as sea surface temperature, salinity, or mixed layer thickness that is relevant to our project. The latter two are extracted from this data source into our composite dataset, whose data is resampled and interpolated using arithmetic mean to fit in our collection resolution from the original $1/12^\circ$ horizontal resolution (Jean-Michel et al., 2021).

Salinity We used in-situ salinity covered at the most shallow point on the elevation range at 0.49 meters below the surface with bias reduced using 3D-VAR scheme correction (Jean-Michel et al., 2021). During coastal upwelling in the West Indian Ocean, subsurface water, which is more salined, rises up to the surface, bringing additional salinity to the surface water which is diluted by heavy precipitation in the monsoon season (Awo et al., 2022; Sreenath et al., 2022). Note that this is not always the case. For example, the Coast of Bengal, where river discharges and rainfall combined created a thick barrier and shallow mixed layer, preventing salinity to reach the surface (Vinayachandran et al., 2002; Lahiri and Vissa, 2022). Despite that, coastal upwelling still occurs in the area with the aid from the impact of seasonal monsoon (Ray et al., 2022). Note that the Coast of Bengal is not covered in our region of interest, so any concerns about the outcome of this variable is to not confused with the inherit nature of the area.

Ocean Mixed Layer Thickness Defined by Sigma T During our search of possible variables to add in our blended dataset product, we came accross Bessa et al. (2019)’s paper in which the author discovered that there is a month by month variability in the mixed layer depth that coincides with the trend of upwelling and downwelling in the Moroccan Atlantic coast. Further research found speculation towards the relationship between the two variables in the Arabian Sea of our region of interest. In Copernicus terms, it is defined as “the ocean depth at which sigma-theta has increase by $0.01 km/m^3$ relative to the near surface value at 10m depth” (Mladek, 2019). Sigma-delta is defined as “water potential density (the density when moved adiabatically to a reference pressure) of water having the same temperature and salinity, minus 1000 kg m-3” (CF Conventions, n.d.).

3.1.3 Global Ocean Colour (Copernicus-GlobColour), Bio-Geo-Chemical, L4 (monthly and interpolated) from Satellite Observations (1997-ongoing)

The Ocean Colour Thematic Assembly Centre (OCTAC) currently provide global and regional high quality data products used by mostly intergovernmental bodies and EU institutions, focusing on mostly ecosystem model assimilation and validation (European Union-Copernicus Marine Service, 2022). The Global Ocean Colour dataset (code name OCEAN-COLOUR_GLO_BGC_L4_MY_009_104), based on data validated using the GlobColour processor owned by Copernicus, output daily and monthly data on a $4km \times 4km$ spatial resolution covering data from September 1997. This wide temporal extent provide our machine learning tasks with plentiful data to train and validate with, and better cover the extensive range that the ERA5 variables do comparing to comparable datasets such as NASA’s MODIS-Aqua (NASA Ocean Biology Processing Group, 2015).

Chlorophyll-a concentration and uncertainty When upwelling happens, we can also observe an increase in nutrient-rich near-surface waters (Benazzouz et al., 2014), in which wind (convective) mixing and upwad nutrient fluxes to the subsurface zone leads to phytoplankton bloom and chlorophyll-a production (Lahiri and Vissa, 2022; Brock et al., 1991). Cold waters being mixed rise above the thermocline to the surface, promoting the growth of species in unfavorable environments, which also contains chlorophyll-a (Alvarez et al., 2010). Therefore, high chlorophyll-a concentrations at the sea surface level can imply whether upwelling is happening. However, based on empirical data processing, we noticed that there is a lot of missing data, which is also confirmed in Park et al. (2020)’s paper. Many factors are weighed in, including phytoplankton’ photosynthetic parameters, seawater optical complexity, or fog and clouds persistence due to seasonal monsoon, leading to rain. S. Yu et al. (2022)’s dataset, while addressed this issue, does not issue a daily resolution dataset that we need to incorporate into our product. Therefore, we resorted to Global Ocean Colour dataset.

3.1.4 Global Ocean Gridded L4 Sea Surface Heights And Derived Variables Reprocessed 1993 Ongoing

The dataset (code name SEALEVEL_GLOB_PHY_L4_MY_008_047) is part of the Sea Level Altimeter product family, providing multiyear records of sea surface height anomalies and derived variables for the whole global ocean (European Union-Copernicus Marine Service, 2021). It has a $0.25^\circ \times 0.25^\circ$ spatial resolution, similar to the standard ERA5’s that we based on, and covered an impressive temporal range from 1993 to 2022.

Sea surface height above geoid and sea surface height above level (sea level height anomaly) Wind components may be a good starting point to investigate the state of coastal upwelling, but comparing to sea surface height anomaly, the latter is more directly involved, through changes in the the thermocline and isothermal layer depth changes (Zhang and Mochizuki, 2022; L. Yu, 2003). We have been searching to no avail for public D20 (20°

isothermal layer depth) or D20 anomaly dataset that satisfies our resolution and coverage requirements. Zhang and Mochizuki (2022) calculated this variable using monthly ocean temp data, but no specific formulae/method is disclosed. We resort to sea surface height anomalies data as the variable is somewhat related to the former variable itself, albeit not completely linear due to complex involvements of other variables in our blended data product, like salinity and temperature (L. Yu, 2003).

3.1.5 Ocean Surface Current Analyses Real-time (OSCAR) Version 2.0

OSCAR uses sea surface height anomaly from the above dataset to compute and analyze the surface current components we are using in our product (Dohan, 2021). In fact, the Global Ocean Gridded L4 dataset also included those variables; however, since we discovered OSCAR first, we have already processed this data before knowing the existence of the other one.

Vertical and horizontal components of surface currents and geostrophic surface currents There are many papers discussing the correlation of currents, especially surface currents, and coastal upwelling (Lentz and Chapman, 2004; Nigam et al., 2018). Rao et al. (2008) mentioned how certain surface current directions (in the case of West Indian Ocean, southernly) would be favourable to the phenomenon. Somalia currents, the surface current in the western Arabian Sea of our interested region, has positive influences to upwelling (Schott et al., 1990). Geostrophic currents, defined as currents balanced between the Coriolis effect forces and gradient pressure forces, are found to contribute greatly to upwelling in systems such as the California Current Systems or Arafura Sea in Indonesia (Ding et al., 2021; Umaroh et al., 2017). By including both non-geostrophic and geostrophic currents, we hope to identify how using the two difference types of currents may impact the model’s productivity, indicating whether it is better to use one variable or the other, or both.

3.1.6 Multiscale UltraHigh Resolution Level 4 Dataset Version 2 (MUR)

The Group for High Resolution Sea Surface Temperature (GHR SST) produced The Multiscale Ultrahigh Resolution (MUR) Level 4 dataset as an interpolated analysis project from multiple satellite instruments to finally achieve an ultra fine-detailed $0.01 \times 0.01^\circ$ spatial resolution covering many variables (NASA/JPL, 2015). We collected sea surface temperature data from this dataset to train an upwelling detection model, and only this model. As we had to weight off its exceptional resolution for a heavy data file and shorter time coverage than ERA5’s, therefore, this dataset is not included in our blended dataset. It is instead provided as a separate subsetted product that covers our region of interest.

3.1.7 SRTM30+ Global 1-km Digital Elevation Model Version 11: Bathymetry

A product from the Scripps Institution of Oceanography of the University of California San Diego, the SRTM30_Plus’s bathymetry data is based on a satellite-gravity model with

a heavily calibrated gravity-to-topography ratio from over two hundred millions soundings (Becker et al., 2009). Given the ultrahigh resolution and precision of the map, we subsetting and provided two bathymetry maps covering our region of interest with different resolutions, one with standard $0.25^\circ \times 0.25^\circ$, and another one with finer resolution using as a basemap/map background due to any graphing of the variables. The former one is included in our final assembled product, and therefore easier to extract and use within the scope of the dataset (which means, we can extract the bathymetry value at a predetermined point right away without having to interpolate from an outside source import).

Bathymetry There have been multiple studies on the relationship between coastal upwelling, such as Garvine (1973) or Lill (1978). They proposed that the ocean depth (and inherently the ocean floor shape or bathymetry) can determine the motion of the subsurface return flow, one of the two principle layers of the upwelling motion of homogeneous water. The topographic variation also influences the water circulation, such as disrupting or redirecting flows along coasts, weakening them, or increasing their strength to enhance mixing (Pitcher et al., 2010).

3.2 Zarr Format

Zarr, short for “zarr array,” is a storage format specifically designed for efficient, scalable, and parallelizable access to multi-dimensional typed arrays (tensors), making it an ideal choice for managing Earth observation data, especially for cloud-hosted data (cite gowen (Moore et al., 2023)). It is developed as an open-source project by using referencible associated metadata and binary data called “chunks” stored in “formatted” directories, it leverages modern data storage technologies, such as chunked and compressed arrays, to optimize storage and retrieval, and reducing access latency.

Gobet and Lane (2012), in their “Encyclopedia of the Sciences of Learning,” referred to “chunk” as a high-level, “meaningful unit of information built from smaller pieces of information.” Therefore, chunking is the mechanism, or the process of creating those objects. While Miller (1956) introduced the term in his 1956 paper as a way of “breaking up long strings of information into units”, it is not until de Groot, in his study of chess experts and observed this phenomenon in nature, developed the concept as a mean of transforming information after observing their capabilities to retain precise brief information on presented chess positions (Frey & Adesman, 1976). Further research explores the concept as a measurement of human cognitive system, and how chunking can be interpreted as an automatic learning processing to “recode information in a more efficient way” (Gobet & Lane, 2012). This definition can somewhat explain the overall concept of chunking in informatics (the field of information), given how it essential divides large datasets into manageable blocks (comparable to “recode information” or more technically speaking, “encoding”). In the Xarray library we mostly used in this project, chunking, by default, is mostly handled by the underlying Dask arrays, where NumPy (or NumPy-like) arrays are broken down and rearranged to speed up certain algorithms (Hoyer et al., 2022; Dask Development Team, 2016).

Resulted chunks then are mapped to metadata files in JSON (JavaScript Object Notation) so that the overall structure and content description can be read quickly (Vance et al., 2019; Miles et al., 2023).

Therefore, understanding chunking, as a mechanism, is crucial in understanding how Zarr works so that it can provide seamless access to very large datasets, often in the terabyte and petabyte range. Additionally, its support for chunked storage, data compression over deduplication, and lightweight metadata management optimizes storage, enables parallel processing, and minimizes access latency, all of which are critical when dealing with extensive datasets which we will incorporate from the above data sources (Miles et al., 2023).

Zarr’s special structure makes it ideal to be stored on the cloud (Pollack, 2023). As modern data storage technologies and strategies, including distributed storage systems and cloud-based solutions, play a crucial role in efficiently managing and accessing large datasets, cloud-based datasets can ensure researchers that they can work with these data resources effectively.

By consolidating our data sources into a Zarr file, we aimed to create an easy-to-use analysis-ready data cube, bringing together multiple diverse datasets onto the same grid for seamless integration. This preprocessing step not only harmonized the data but also ensured that it adhered to a consistent spatial and temporal framework, facilitating efficient and comprehensive analyses of Earth’s oceans. This approach aligns with the broader shift in the remote-sensing community towards providing researchers with analysis-ready datasets, thus enabling more accessible and reproducible scientific investigations.

3.3 Data Blending and Processing

3.3.1 Computed Variables

To alleviate the usage of the product, we also pre-computed absolute speed and direction using vertical and horizontal components of our wind and (near-)surface current variables. For speed, we utilized a simple Pythagorean theorem approach where

$$v = \sqrt{v_x^2 + v_y^2} \quad (1)$$

with v as vector-less speed, and v_x and v_y as horizontal and vertical velocity components, respectively. For direction, we utilized NumPy’s `arctan2()` function and then convert radians to degrees using their `rad2deg()` function, with the latter chosen as degrees are more commonly used in meteorology than radians due to its unique conventions comparing to the standard mathematical Cartesian plane’s (Harris et al., 2020; “Meteorological Conventions”, 2022).

3.3.2 Interpolation

Due to the mismatched spatial grid configurations between our original datasets, we also applied linear interpolation on, both spatially and temporally, on all of our data variables so that they all follow an average daily temporal, $0.25^\circ \times 0.25^\circ$ spatial grid. While temporal

ranges may vary among data sources, with an insistence on available data of at least twenty-one years from 2000-2020, we enforced a spatial range of $-12^{\circ}S \rightarrow 32^{\circ}N$, $42^{\circ}E \rightarrow 102^{\circ}E$ across all variables.

4 Models

4.1 Exploratory Analysis using Unsupervised Learning on SST Data

In order to gain preliminary insights into the patterns of SST data images, an unsupervised learning approach was undertaken. We employed the K-means clustering algorithm (MacQueen, 1967), preceded by feature extraction from the images using the EfficientNetB0 model (Tan & Le, 2020a) and dimensionality reduction using PCA (Jolliffe & Cadima, 2016).

EfficientNetB0 served as the initial sieve, transforming the SST imagery into a form amenable to mathematical scrutiny. By transmuting the raw visuals into a higher-dimensional space, it paved the way for PCA to distill the essence of these features. This reduction in complexity was essential not for computational ease but to hone in on the pivotal variances that truly mattered.

Grounded in past explorations, the choice of three clusters emerged as a pivotal number in K-means clustering. Through exhaustive pattern examination combined with standard K selection heuristics, it became evident that tri-clustering adeptly captured the primary motifs, particularly during pronounced upwelling events.

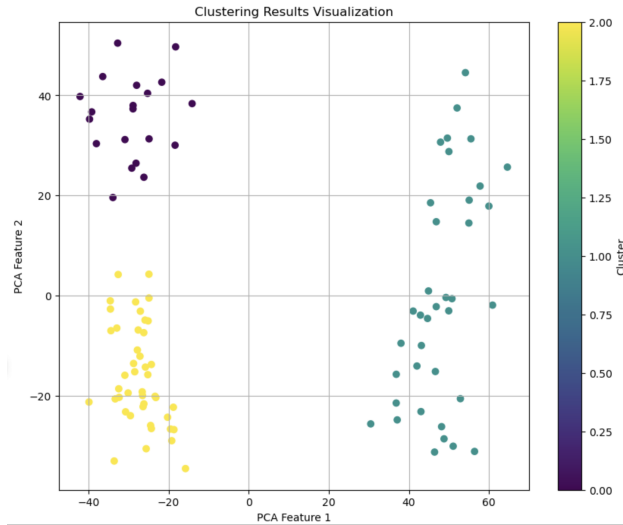


Figure 1: Clusters formed from the SST data visualized in a 2D space using the first two principal components.

These clusters, while providing an overarching view, are not an end but a means. They crystallize dominant trends and anomalies, poised to inform subsequent analytic ventures.

However, the realm of unsupervised methods, while expansive, is not exhaustive. Certain intricacies and subtleties risk being glossed over in such a broad-brush approach.

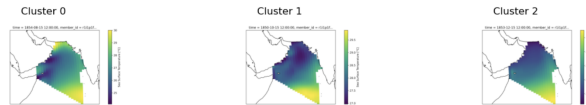


Figure 2: Representative images for each of the clusters.

As we transitioned from this macro-view, it became imperative to delve deeper. The clusters illuminated the path but didn’t delineate it. To tread this path with precision, a shift to supervised methodologies was necessitated, leveraging the synergy between previously unearthed patterns and the specific insights that tailored-modeling on labeled data can confer.

4.2 Supervised Learning

Supervised learning, with its ability to harness labeled data, offers a more targeted mechanism to both model and predict SST values and upwelling events. Traditionally, SST prediction and upwelling detection have been approached using a variety of methods. Common techniques for SST prediction include statistical models (Trenberth & Shea, 1987), machine learning algorithms like support vector machines, and neural networks (Krasnopolsky et al., 2005), while upwelling detection often resorts to heuristic algorithms or threshold-based methods.

However, with the rapid advancement of deep learning, newer models have shown significant achievements in various domains. The Transformer architecture (Vaswani et al., 2023) has been revolutionary in the field of natural language processing, reshaping the way we understand and build models for language tasks. The ConvLSTM (Shi et al., 2015) blends the strengths of convolutional neural networks and recurrent neural networks, proving to be highly effective in sequence-to-sequence predictions. EfficientNet (Tan & Le, 2020b) has gained recognition for its exceptional performance in image classification, scaling in a compound manner to achieve state-of-the-art results. Similarly, U-Net (Ronneberger et al., 2015) stands out in image segmentation tasks, extracting intricate details across various applications.

In this context, our approach presents a departure from traditional methodologies. For SST prediction, we employ the Transformer, ConvLSTM, and an innovative combination of both. In terms of upwelling detection, we explore SST-Based Upwelling Detection in Bounding Box using EfficientNet, delve into Multivariate Upwelling Detection, and utilize the U-Net architecture for precise upwelling segmentation.

The ensuing sections will focus on these techniques in detail, partitioned into two primary segments: SST prediction and upwelling detection.

4.2.1 SST Prediction

Within the ambit of supervised learning, accurate SST prediction holds significant importance. Predicting SST values accurately can illuminate patterns in marine dynamics, including early signs of upwelling events. Such predictions can, in turn, serve as valuable inputs for systems aimed at detecting and potentially forecasting upwelling occurrences. By combining SST prediction and upwelling detection, we position ourselves to better understand, anticipate, and respond to marine phenomena.

Model Architectures and Their Rationale:

- **Linear Model:** The most straightforward approach, it predicts SST based on past linear trends without focusing on complex relationships.
- **Transformer:** Inspired by the seminal "Attention is All You Need" paper, this model capitalizes on self-attention mechanisms to weigh the importance of various data points from the input data. It provides the flexibility to focus on critical temporal patterns while potentially ignoring less relevant information.
- **ConvLSTM:** A fusion of convolutional neural networks (CNN) and Long Short-Term Memory (LSTM) units, ConvLSTM inherently captures spatial and temporal dependencies. However, it's more resource-intensive, with RAM consumption increasing notably with larger input windows.
- **ConvLSTM & Transformer:** An ambitious amalgamation, this model attempts to harness the spatial-temporal prowess of ConvLSTM and the discerning capability of Transformers. It's designed to exploit the strengths of both architectures.

Optimization and Evaluation:

- **Window Size:** Our choice of a 5-day input window is a conscious balance between capturing meaningful SST patterns and ensuring computational feasibility. Especially for models like ConvLSTM, larger windows significantly inflate RAM requirements.
- **Optimizer:** Adam, an adaptive learning rate optimizer, is our choice across models. It combines the best properties of the AdaGrad and RMSProp algorithms to handle sparse gradients on noisy problems. Its adaptive nature ensures efficient convergence and is particularly well-suited for problems like SST prediction, where data can exhibit substantial variability.
- **Loss Function:** After benchmarking Mean Squared Error (MSE), Mean Absolute Error (MAE), and Structural Similarity Index (SSIM), MSE emerged as the most effective for our task. It penalizes larger errors more than smaller ones, ensuring predictions are as close to the true values as possible.

- **Evaluation Criterion:** For each model’s predictions, besides the optimal validation MSE, we compared the MSE between the Predicted Output and the True Output for the 6th day and the MSE between the Last Input Frame (5th day) and True Output. A model is deemed successful if the former is lower than the latter, signifying that the architecture doesn’t merely carry forward the last seen value but genuinely learns and predicts the SST dynamics.

Linear Model

In the early stages of our investigation into predicting SST, we opted for the linear model as our maiden approach. Renowned for its straightforwardness, linear regression seeks to unveil linear relationships within datasets, a reason we considered it an apt initial model for our study.

Operating under the dimensional constraints typical of linear models, we tailored our training to individual geospatial coordinates, focusing on singular points such as latitude 45.0 and longitude -45.0. This methodology was exclusively driven by data from a designated pixel or position within our overarching dataset. While it allowed for pointed analysis, this narrowed lens excluded broader contextual inputs from surrounding pixels. As a result, potentially influential spatial patterns in SST dynamics remained beyond its purview.

Upon deploying this model, our empirical findings were revealing. Although the model generated predictions, their accuracy indicated significant room for refinement. The heightened MSE underscored the limitations of relying on isolated data points for SST predictions. Without the invaluable context provided by adjacent data, it became evident that the intricate dance of factors shaping SST — be it temperature variations in neighboring water areas, overarching climatic shifts, or the nuanced choreography of ocean currents — was conspicuously absent in this model’s considerations.

Such insights gleaned from our linear model experiments emphasized the need for more intricate modeling strategies. A model that synergizes diverse data points could promise more holistic insights, potentially enhancing the accuracy of predictions. As we ventured further, renowned models like Transformers and ConvLSTM, which have achieved commendable success in diverse domains, appeared as promising candidates. These models, with their potential to offer a more encompassing view of SST dynamics, set the stage for our subsequent research endeavors.

Transformer

Following our exploration of linear models, our attention turned to the transformative capabilities of the Transformer architecture (Vaswani et al., 2023). Originally pioneered for sequence-to-sequence tasks, the Transformer’s distinctive self-attention mechanism empowers it to weigh input data variably based on their relevance. This inherent ability to discern importance across a sequence positions the Transformer as a promising candidate for refining the intricacies of SST predictions.

Datasets: For our predictive modeling, we harnessed the SST values from 2018 to 2022 of

our ERA5 dataset.

Model Architecture: The structure of our SST-predictive Transformer is rooted in its MultiHeadAttention mechanism. This unique feature enables the model to concurrently engage with various segments of the input data, granting it a more nuanced and contextual appreciation of SST sequences. Initially, the model flattens the spatial dimensions, setting the stage for the subsequent Transformer blocks. Integrated within these blocks are dropout layers and L2 regularization, both critical in mitigating the risk of overfitting and ensuring the model remains generalizable to unseen data. Following this transformation, the output is reverted to its original spatial structure and subjected to LayerNormalization for added stability. Sequential layers, including a Feed Forward Network (FFN), further refine the normalized output. Conclusively, the architecture employs a GlobalAveragePooling layer, consolidating the temporal aspects, and a decisive decoding phase, reconstructing the data to echo our anticipated SST output shape.

| Layer (type) | Output Shape | Param # | Connected to |
|---|-----------------------|---------|--|
| input_1 (InputLayer) | [(None, 5, 149, 181)] | 0 | [] |
| time_distributed (TimeDistributed) | (None, 5, 26969) | 0 | ['input_1[0][0]'] |
| multi_head_attention (MultiHeadAttention) | (None, 5, 26969) | 5860526 | ['time_distributed[0][0]', 'time_distributed[0][0]'] |
| dropout (Dropout) | (None, 5, 26969) | 0 | ['multi_head_attention[0][0]'] |
| time_distributed_1 (TimeDistributed) | (None, 5, 149, 181) | 0 | ['dropout[0][0]'] |
| tf.__operators__.add (TFOpLambda) | (None, 5, 149, 181) | 0 | ['time_distributed_1[0][0]', 'input_1[0][0]'] |
| layer_normalization (LayerNormalization) | (None, 5, 149, 181) | 362 | ['tf.__operators__.add[0][0]'] |
| time_distributed_2 (TimeDistributed) | (None, 5, 26969) | 0 | ['layer_normalization[0][0]'] |
| dense (Dense) | (None, 5, 256) | 6904320 | ['time_distributed_2[0][0]'] |
| dropout_1 (Dropout) | (None, 5, 256) | 0 | ['dense[0][0]'] |
| dense_1 (Dense) | (None, 5, 181) | 46517 | ['dropout_1[0][0]'] |
| layer_normalization_1 (LayerNormalization) | (None, 5, 181) | 362 | ['dense_1[0][0]'] |
| global_average_pooling1d (GlobalAveragePooling1D) | (None, 181) | 0 | ['layer_normalization_1[0][0]'] |
| dense_2 (Dense) | (None, 26969) | 4908358 | ['global_average_pooling1d[0][0]'] |
| reshape_1 (Reshape) | (None, 149, 181) | 0 | ['dense_2[0][0]'] |

Figure 3: Transformer Model Summary

ConvLSTM

Emerging from the foundational understanding rendered by linear models and the strategic insights of the Transformer, we ventured into the world of ConvLSTM—an architecture tailored for sequential data (Shi et al., 2015). The allure of the ConvLSTM resides in its ability to reconcile the spatial understanding that convolutional neural networks (CNNs) offer with the temporal acumen intrinsic to Long Short-Term Memory Networks (LSTMs). Thus, marrying the strengths of both paradigms, the ConvLSTM brings forth a synergistic approach that could holistically fathom the depths of SST dynamics.

Datasets (We trained the same ConvLSTM model architecture on two different datasets):

- ERA5 Dataset (2000-2022)
- MUR Dataset (2010-2017)

Model Architecture: Our foray into the ConvLSTM landscape brought about an architecture that begins its journey with a foundational ConvLSTM2D layer. Pivotal in digesting the spatiotemporal intricacies of the SST data, this layer is fortified with 32 filters, each of size 3×3 , ensuring comprehensive coverage of the input shape, with padding retained for spatial consistency. With the incorporation of Batch Normalization—a tool instrumental in stabilizing neural activations—and a 30% dropout for regularization, the foundational layer hands over the torch to subsequent convolutional layers. The following layers—two Conv2D layers in tandem—augment the spatial comprehension. Both layers possess a kernel size of 3×3 , with the first one boasting 64 filters and the subsequent one hosting 32, ensuring that the spatial features are progressively distilled. Each of these layers, apart from being regularized through Batch Normalization and Dropout, culminates in ReLU activations, providing the necessary non-linearity. The architectural journey concludes with an output layer, a Conv2D, which ensures that the final predictions align with the desired spatial configuration. Its linear activation, coupled with a kernel size of 3×3 , provides predictions that are both granular and accurate.

| Layer (type) | Output Shape | Param # |
|---|----------------------|---------|
| conv_lstm2d (ConvLSTM2D) | (None, 401, 451, 32) | 38144 |
| batch_normalization (Batch Normalization) | (None, 401, 451, 32) | 128 |
| dropout (Dropout) | (None, 401, 451, 32) | 0 |
| conv2d (Conv2D) | (None, 401, 451, 64) | 18496 |
| batch_normalization_1 (Batch Normalization) | (None, 401, 451, 64) | 256 |
| dropout_1 (Dropout) | (None, 401, 451, 64) | 0 |
| conv2d_1 (Conv2D) | (None, 401, 451, 32) | 18464 |
| batch_normalization_2 (Batch Normalization) | (None, 401, 451, 32) | 128 |
| dropout_2 (Dropout) | (None, 401, 451, 32) | 0 |
| conv2d_2 (Conv2D) | (None, 401, 451, 1) | 289 |

Figure 4: ConvLSTM Model Summary

ConvLSTM & Transformer

In the realm of temporal sequence data modeling and based on our previous experiments, ConvLSTM has stood out as a robust architecture, capable of capturing the spatial and temporal dynamics inherent to such data. However, with the rise of the Transformer architecture, primarily known for its prowess in handling sequential data in the natural language processing domain, we were intrigued to investigate its potential synergies with ConvLSTM in our specific use case.

The Transformer model, with its unique attention mechanism, can give variable importance to different parts of an input sequence, thus potentially capturing intricate spatial-temporal patterns that might be missed by ConvLSTM alone. When combined, the ConvLSTM can ensure the spatial context is preserved, while the Transformer layer can ensure that the model pays attention to the most critical parts of the input sequence. This amalgamation brings the best of both architectures, where spatial relationships are maintained, and variable importance to temporal sequences is assigned.

Datasets: For this innovative combination, we leveraged the ERA5 dataset, but only for the year 2020. The decision to narrow down to one year was primarily due to the substantial computational memory demands of the hybrid architecture.

Model Architecture: Venturing into a hybrid ConvLSTM-Transformer model, we initiated our design with a ConvLSTM2D layer, equipped with 16 filters of a 3x3 dimension, ensuring detailed processing of the input with spatial consistency through padding. Following this, Batch Normalization optimizes activation dynamics, subsequently undergoing a zero-padding to cater to a MaxPooling2D layer, which emphasizes salient features. As the architecture’s journey evolves, the reshaped data interfaces with the multi-headed attention mechanism of the Transformer—facilitating intricate inter-relational learning, reinforced by residual connections. The model then employs layer normalization, interwoven with sequential operations, to effectively capture temporal hierarchies. A subsequent up-sampling returns the data to its spatial essence, setting the stage for a final Conv2D layer, culminating our endeavor to harness the combined might of ConvLSTM’s spatiotemporal prowess with the Transformer’s relational finesse.

| Layer (type) | Output Shape | Param # | Connected to |
|---|--------------------------|---------|---|
| input_1 (InputLayer) | [(None, 5, 149, 181, 1)] | 0 | [] |
| conv_lstm2d (ConvLSTM2D) | (None, 149, 181, 16) | 9856 | ['input_1[0][0]'] |
| batch_normalization (Batch Normalization) | (None, 149, 181, 16) | 64 | ['conv_lstm2d[0][0]'] |
| zero_padding2d (ZeroPadding2D) | (None, 150, 182, 16) | 0 | ['batch_normalization[0][0]'] |
| max_pooling2d (MaxPooling2D) | (None, 75, 91, 16) | 0 | ['zero_padding2d[0][0]'] |
| reshape (Reshape) | (None, 6825, 16) | 0 | ['max_pooling2d[0][0]'] |
| multi_head_attention (MultiHeadAttention) | (None, 6825, 16) | 2160 | ['reshape[0][0]', 'reshape[0][0]', 'reshape[0][0]'] |
| add (Add) | (None, 6825, 16) | 0 | ['multi_head_attention[0][0]', 'reshape[0][0]'] |
| layer_normalization (Layer Normalization) | (None, 6825, 16) | 32 | ['add[0][0]'] |
| sequential (Sequential) | (None, 6825, 16) | 1072 | ['layer_normalization[0][0]'] |
| add_1 (Add) | (None, 6825, 16) | 0 | ['sequential[0][0]', 'layer_normalization[0][0]'] |
| layer_normalization_1 (Layer Normalization) | (None, 6825, 16) | 32 | ['add_1[0][0]'] |
| reshape_1 (Reshape) | (None, 75, 91, 16) | 0 | ['layer_normalization_1[0][0]'] |
| up_sampling2d (UpSampling2D) | (None, 150, 182, 16) | 0 | ['reshape_1[0][0]'] |
| cropping2d (Cropping2D) | (None, 149, 181, 16) | 0 | ['up_sampling2d[0][0]'] |
| conv2d (Conv2D) | (None, 149, 181, 1) | 145 | ['cropping2d[0][0]'] |

Figure 5: ConvLSTM & Transformer Model Summary

4.2.2 Upwelling Detection

Building on our work with SST predictions, we ventured into another significant domain of oceanographic studies: upwelling detection. Our approach leverages the differences in SST between proximate coastal zones and distant oceanic regions. By delineating two sets of reference points along specified coastal buffer zones, we set the stage for a nuanced understanding of temperature gradients indicative of upwelling events. The primary set, termed as near shore points, was strategically positioned approximately 50km from the coastline, while the secondary set, termed offshore points, was placed about 300km away from the shoreline.

To derive precise SST data from our datasets, a bespoke algorithmic approach was employed. This algorithm pinpoints the closest dataset point for each of our reference points, guaranteeing that the obtained SST values are both geographically apt and accurate. With the data in hand, our methodology then hinges on calculating the SST differential between the paired near-shore and offshore points. By determining the difference in temperature between these two points — subtracting offshore SST values from the near-shore ones — we derived a metric for the temperature gradient. Setting a clear criterion, with SST differentials less than -1 pointing towards upwelling, we efficiently labeled regions experiencing upwelling.

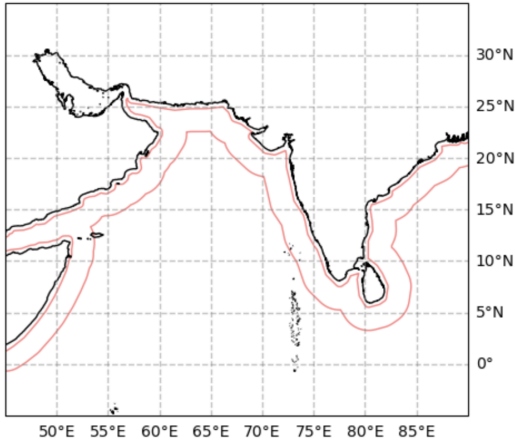


Figure 6: Marked 50 km and 300 km Lines Offshore

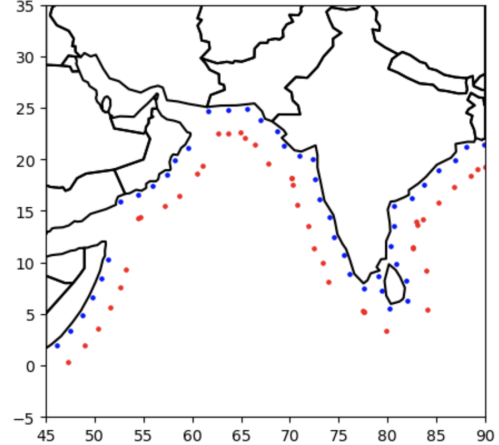


Figure 7: Near Shore Points (Blue) and Off Shore Points (Red)

SST-Based Upwelling Detection in Bounding Box using EfficientNet

Given the intricate spatial dynamics of upwelling events, our approach began by focusing on the holistic behavior of the bounding box. Using representative points from the near shore dataset, specifically the 22nd and 23rd points, we formulated a criterion for upwelling detection. If the SST difference for both these points, when compared with their respective offshore counterparts, was less than -1, the entire bounding box was determined to exhibit upwelling. This streamlined our task into a straightforward binary classification: labeling bounding boxes as either 0 (no upwelling) or 1 (upwelling detected).

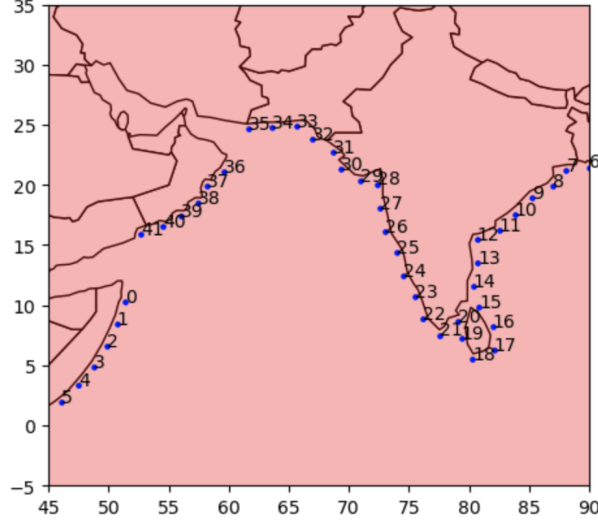


Figure 8: Near Shore Points with Indexes

To achieve this classification, we employed the EfficientNet architecture (Tan Le, 2019). We utilized the EfficientNetB0 variant, modifying its architecture to align with our problem statement by removing its top layer. Subsequent layers, such as GlobalAveragePooling2D, a 1024-node fully connected layer, and a final logistic layer, were added. Given EfficientNet’s classification capabilities, we set an empirical threshold at 0.5, beyond which the occurrence of upwelling is predicted.

Multivariate Upwelling Detection

In our pursuit of a more refined upwelling detection model, we systematically integrated an array of variables: SST, air temperature, wind speed, and wind direction. SST, as a widely accepted determinant, offers essential insights into upwelling phenomena (Trenberth & Shea, 1987). Meanwhile, expanding the model to encompass additional variables, such as air temperature (Deser et al., 2010), wind speed, and wind direction (Bakun, 1990), was strategically pursued to achieve heightened predictive precision by capturing a holistic view of marine and atmospheric conditions.

Our approach utilized an ensemble of EfficientNetB0 architectures, each dedicated to processing one of the aforementioned variables: The SST data was processed by a dedicated EfficientNetB0 model. A separate model was allocated for air temperature analysis. Wind speed and wind direction were each processed by their respective EfficientNetB0 models. Post convolution, GlobalAveragePooling2D layers distilled the outputs of these models into concatenated feature vectors. A subsequent dropout layer was introduced to minimize overfitting. This combined feature set was then processed through a dense layer and culminated in a logistic output layer predicting upwelling occurrences.

Segmentation with U-Net for Upwelling Detection

Having employed EfficientNet models to pinpoint potential upwelling events within bounding

boxes, the next crucial step is to decipher the exact spatial locations of these events within those confines. For this precise task, a segmentation model known as U-Net (Ronneberger et al., 2015) was chosen, largely due to its prowess in biomedical image segmentation. The U-Net architecture implemented consists of an encoding path that captures the context and a decoding path that enables precise localization. In our adapted architecture, the encoder comprises two convolutional blocks followed by max-pooling operations to down-sample the feature maps. Conversely, the decoder upsamples the feature maps and merges them with high-resolution features from the encoder to recover spatial information.

| Layer (type) | Output Shape | Param # |
|------------------------------------|-----------------------|---------|
| input_1 (InputLayer) | [(None, 149, 181, 1)] | 0 |
| conv2d (Conv2D) | (None, 149, 181, 64) | 640 |
| max_pooling2d (MaxPooling2D) | (None, 74, 90, 64) | 0 |
| conv2d_1 (Conv2D) | (None, 74, 90, 128) | 73856 |
| conv2d_transpose (Conv2DTranspose) | (None, 148, 180, 64) | 32832 |
| zero_padding2d (ZeroPadding2D) | (None, 149, 181, 64) | 0 |
| conv2d_2 (Conv2D) | (None, 149, 181, 64) | 36928 |
| conv2d_3 (Conv2D) | (None, 149, 181, 3) | 195 |

Figure 9: U-Net Model Summary

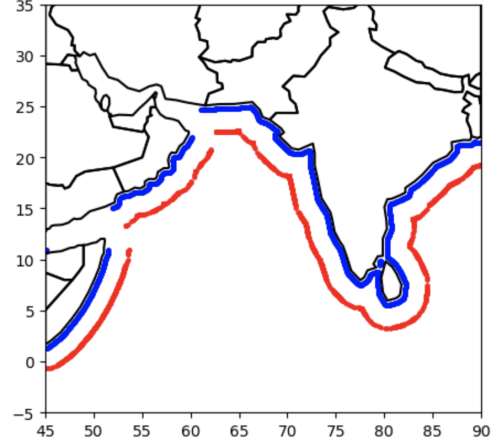


Figure 10: Densely Packed Near Shore Points (Blue) and Off Shore Points (Red)

For the training of the U-Net model, our data underwent rigorous preprocessing. We leveraged SST data, where regions denoting land (indicated by NaN values in the SST data) were labeled as 0. The expansive oceanic areas devoid of upwelling activity received a label of 1. Crucially, the locations manifesting upwelling phenomena were distinguished with a label of 2. To assign this label, we initially identified pairs of points – one near the shore and the other offshore – in a much denser configuration than our previous approach (see Figure 16). By examining the SST difference between these paired points, we inferred potential upwelling events. We then harnessed the Bresenham line algorithm (Bresenham, 1965) to trace a line between these pairs, marking the entire line’s trajectory as upwelling regions. In essence, this technique effectively translated geographical coordinates into their corresponding indices in our dataset, ensuring a comprehensive representation of upwelling locations.

5 Results

5.1 SST Prediction

5.1.1 Transformer

In our training regimen, by the 12th epoch, the model produced a loss of 0.1798 with an MSE of 0.0937. On our validation set, the loss rose to 0.2814, and the MSE settled at 0.1902. Visually examining the predictions, it became evident that the Transformer exhibited competence in capturing overarching SST trends, yet faced challenges in delineating finer details. A pertinent observation arose when comparing the Mean Squared Error (MSE) values. The MSE for the predicted output compared to the true output was generally higher than that of the last input frame compared to the true output. This underlined that our Transformer’s predictions, although promising, were not yet on par with the benchmark set by the last input frame.

5.1.2 ConvLSTM

By the time the model reached its 10th epoch during the training process on the ERA5 dataset, it exhibited a training MSE of 0.0454 and a commendable validation MSE of 0.0271. In contrast, when processing the MUR dataset, the model’s metrics by the 20th epoch showcased a training MSE of 0.0764 complemented by a validation MSE of 0.0480. It’s noteworthy that while the ERA5 dataset steered the model towards a reduced validation MSE at its concluding epoch, it consistently registered a higher MSE between the Predicted Output and the True Output as compared to its MSE between the Last Input Frame and the True Output. Conversely, the MUR dataset, despite its initial semblance of a higher error, consistently delivered results where the MSE between Predicted Output and True Output was invariably lesser than the corresponding MSE between Last Input Frame and True Output. This aligns seamlessly with our set objectives and underscores the significance of dataset nuances in model performance. Figure 15 below shows an example depicting the difference between the predicted and true sst data using our ConvLSTM model trained with the MUR dataset:

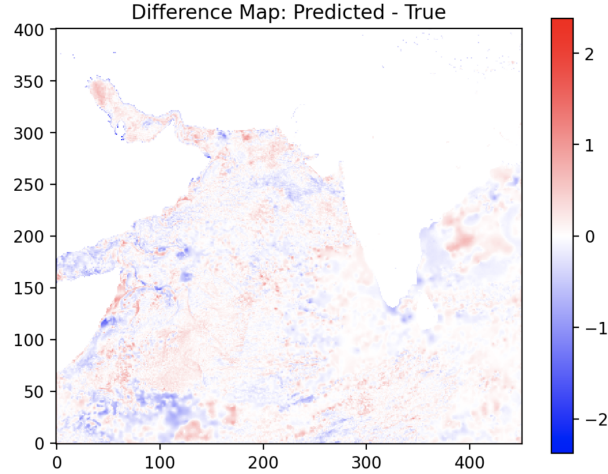


Figure 11: Difference between the Predicted and True SST Data for 2023-09-06

5.1.3 ConvLSTM & Transformer

By the conclusion of the 20th epoch, our model reported a training mean squared error (MSE) of 0.0498 and a validation MSE of 0.0493. Notably, the early stopping mechanism was never activated during training, underscoring the consistent learning trajectory of our model. In terms of its predictive prowess, the MSE between the Predicted Output and True Output was marginally higher than that between the Last Input Frame and True Output. Although this discrepancy suggests a slightly diminished performance compared to a pure ConvLSTM approach, it's essential to highlight the model's significant potential. This perspective is grounded in the fact that the training was exclusively based on a single year's worth of data without triggering early stopping.

5.1.4 Extensions of Our ConvLSTM Model

Dynamic Bounding Box with ConvLSTM Moving from our past efforts with fixed bounding boxes, our recent approach adopts a flexible design to accommodate varying spatial dimensions in SST prediction. Our traditional models, though effective, were confined to a predetermined spatial shape. This posed issues when dealing with datasets of different resolutions. To address this, we introduced a dynamic architecture.

Our advanced ConvLSTM model excels in adaptability, accommodating SST data of any spatial size. It's crucial to note that identical geographical datasets can differ in dimension due to resolution variations, underscoring our model's flexibility. Describing the architecture briefly, it begins with a ConvLSTM layer capable of dynamic spatial inputs. Subsequent layers, comprising two Conv2D layers enhanced with Batch Normalization and Dropout, refine the spatial details. The model concludes with an output layer for final SST predictions.

Overall, our dynamic ConvLSTM merges flexibility and performance, offering a solution for diverse resolution datasets, underscoring its significance in SST prediction.

Table 1: Summary of Models

| Model | Training MSE | Validation MSE | Predicted MSE < Last Input MSE |
|-------------------------|------------------------|------------------------|--------------------------------|
| Transformer | 0.0937 (12th epoch) | 0.1902 (12th epoch) | False |
| Convlstm (ERA5 dataset) | 0.0454 (10th epoch) | 0.0271 (10th epoch) | False |
| Convlstm (MUR dataset) | 0.0764 (20th epoch) | 0.0480 (20th epoch) | True |
| Convlstm & Transformer | 0.0498 (20th epoch) | 0.0493 (20th epoch) | False |

| Layer (type) | Output Shape | Param # |
|---|------------------------|---------|
| conv_lstm2d (ConvLSTM2D) | (None, None, None, 32) | 38144 |
| batch_normalization (Batch Normalization) | (None, None, None, 32) | 128 |
| dropout (Dropout) | (None, None, None, 32) | 0 |
| conv2d (Conv2D) | (None, None, None, 64) | 18496 |
| batch_normalization_1 (Batch Normalization) | (None, None, None, 64) | 256 |
| dropout_1 (Dropout) | (None, None, None, 64) | 0 |
| conv2d_1 (Conv2D) | (None, None, None, 32) | 18464 |
| batch_normalization_2 (Batch Normalization) | (None, None, None, 32) | 128 |
| dropout_2 (Dropout) | (None, None, None, 32) | 0 |
| conv2d_2 (Conv2D) | (None, None, None, 1) | 289 |

Figure 12: Flexible ConvLSTM Model Summary

Iterative Predictions Using ConvLSTM: Building on the foundations laid by the dynamic ConvLSTM architecture, we ventured into implementing an iterative prediction strategy on the MUR dataset. In this methodology, a sliding window approach is employed, wherein the model leverages data from the past five days to generate predictions for the immediate next day. Once the prediction for the sixth day is procured, the model recalibrates its input by shifting the window: it drops the first day, includes the second to fifth days, and incorporates the recently predicted sixth day to prognosticate the seventh day. This iterative process continues, effectively allowing the model to generate forecasts for an extended time horizon beyond just a single day.

The empirical results, acquired from September 2021, substantiate the efficacy of this approach. A comparative assessment between the Mean Squared Error (MSE) values of the predictions and the natural progression of days (i.e., the MSE between the last observed day in the sequence and the actual next day) reveals a consistent trend: the predicted MSE values were invariably lower than the natural MSE values. This differential underscores the proficiency of the model, suggesting that its predictions were not only closer to the actual values but also consistently so across the tested period.

The initial results from this study are promising. It suggests that the model has the potential not just in forecasting immediate short-term SST values, but might also be able to iteratively predict over extended durations. Sea surface temperature dynamics are influenced by a plethora of factors, and achieving accurate multi-day predictions, even if preliminary, offers a glimpse into potential future advancements in our SST prediction research.

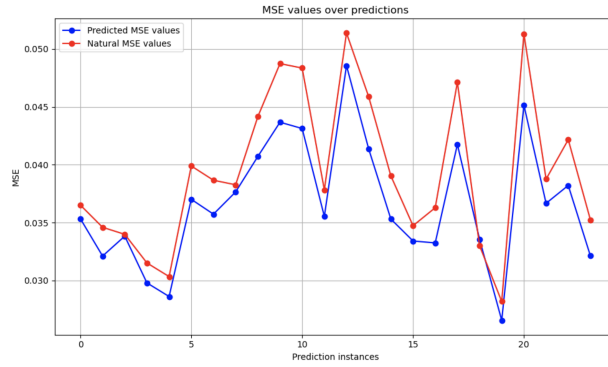


Figure 13: MSE Values Over Predictions for September, 2021

5.2 Upwelling Detection

5.2.1 SST-Based Upwelling Detection in Bounding Box using EfficientNet

Having delineated the EfficientNet model architecture, we now pivot to evaluate its empirical performance. Our model was trained using the Adam optimizer with a binary cross-entropy loss function. Evaluation of our dataset revealed a test accuracy of approximately 97.87%, underscoring its effectiveness in discerning upwelling events within the bounding boxes. From Figure 13, it can also be observed that the predicted upwelling days from 2000 to 2020 all fall between June and October, which aligns with the typical upwelling season observed during the Southwest Monsoon in the Arabian Sea (Wiggert et al., 2006).

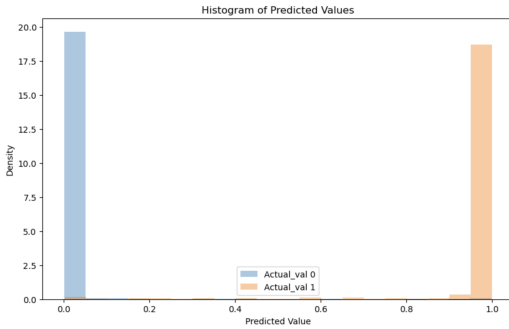


Figure 14: Histogram of Predicted Values

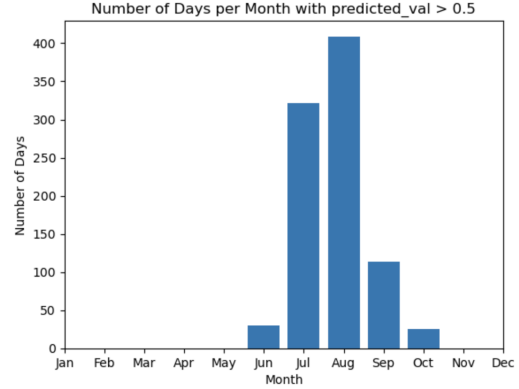


Figure 15: Distribution of days that upwelling happens if using a threshold of 0.5

5.2.2 Multivariate Upwelling Detection

The results from the multivariate approach were promising. Our model achieved a test accuracy of 98.45%, marking an improvement from the 97.87% accuracy achieved with SST alone. This increment underscores the importance of a holistic multivariate approach in upwelling detection.

5.2.3 LIME Interpretation of the EfficientNet Model

In the realm of deep learning, understanding the decision-making process of complex models is often challenging, given their "black-box" nature. To shed light on the internal dynamics of our EfficientNet model, we employed the LIME (Local Interpretable Model-agnostic Explanations) framework (Ribeiro et al., 2016), a tool designed to provide interpretable insights for any machine learning model.

Our approach commenced by segmenting the image. The SLIC (Simple Linear Iterative Clustering) algorithm (Achanta et al., 2012) was utilized, partitioning the image into approximately 200 compact segments. This segmentation aids in understanding which specific regions of the image the model deems significant for its predictions.

With the segmented image, the LIME explainer was applied. LIME works by perturbing the image, and creating multiple interpretable data samples around it. The model's predictions on these samples are then used to fit a locally interpretable model, which approximates the decision boundaries of the EfficientNet model. By analyzing these decision boundaries, we obtain a mask highlighting the influential segments that led the model to its conclusion.

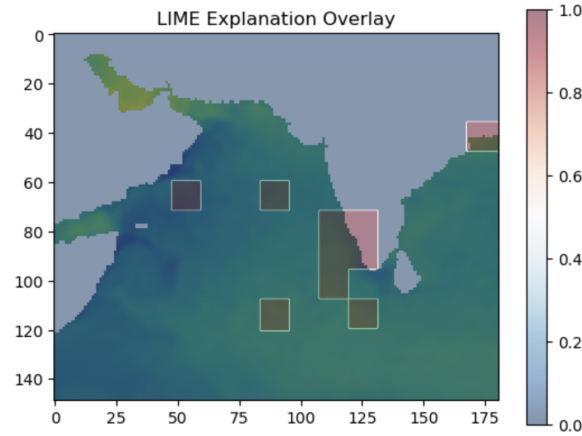


Figure 16: Lime Interpretation for Our EfficientNet Model using 2018-07-15's SST Data

The outcome of this interpretative exercise was a visual overlay on the original image, showcasing the regions of significance. Through this LIME explanation, not only do we gain a deeper understanding of the model's focal points, but we also achieve a measure of confidence in its predictions, as we can correlate its decisions with known oceanographic phenomena.

In essence, LIME interpretation acts as a bridge, connecting the intricate computations of a deep learning model to the tangible realities of the environment it aims to understand.

5.2.4 Segmentation with U-Net for Upwelling Detection

Using Adam as the optimizer and sparse categorical cross-entropy as the loss function, the model demonstrated commendable performance. The convergence was monitored using early stopping based on validation loss to prevent overfitting. Upon completion of the detailed training regimen, the U-Net model exhibited notable performance. It achieved an impressive accuracy of 99.71% on the training set and mirrored this result with a 99.71% accuracy on the validation set. These metrics not only vouch for the model's adeptness at distinguishing between land, ocean, and upwelling events but also underscore the potency of U-Net in geospatial image segmentation tasks.

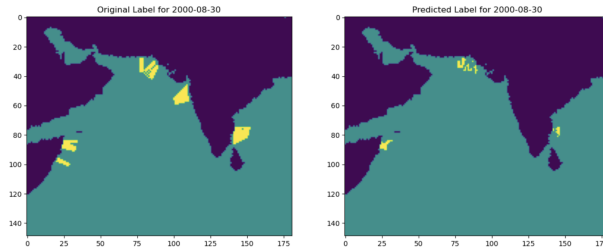


Figure 17: True Label and U-Net Prediction for 2000-08-30

However, a purely numerical assessment doesn't capture the full picture. Observations from the actual visual outputs of the model revealed some disparities between its predictions and the true labels, especially in the finer details. There were areas, particularly within intricate upwelling regions, where the model seemed to miss some nuances present in the real scenario. Such oversight in capturing minute details might have ramifications in real-world applications and warrants further attention.

Regardless, venturing to apply the U-Net model for upwelling detection remains an exploratory move. From the outcomes thus far, it's evident that this direction holds promise. The choice of the U-Net architecture resonates with its proven track record in other image segmentation domains and its potential benefits in handling geospatial data. Yet, as with any pioneering endeavor, the model undoubtedly requires additional fine-tuning and refinements to further boost its precision in upwelling detection.

6 Limitations

In our pursuit to detect upwelling phenomena using various deep learning architectures, certain limitations emerged that merit attention. On behalf of the data processing side, we noticed that there are some potential variables worth testing out that have strong correlations to coastal upwelling such as wind stress or D20 anomalies, but could not be included due to a considerable shortage of temporal coverage and/or low resolution (Lentz and Chapman (2004); Zhang and Mochizuki (2022)). Additionally, not all of our data variables may not correlate to state of upwelling instantly. For example, despite upwelling occurred in both the southeast and northeast Arabian sea, subsurface water only reached the surface in the latter region, which may cause issues in predictions using near-surface salinity concentration as a variable (Lahiri & Vissa, 2022). Phytoplankton blooms may also delay open-sea upwelling, calling into question the precision of chlorophyll-a concentrations (Brock et al., 1991). Remote sensing data may also not be accurate (or sometimes even missing), as per the case of the mentioned variable (Park et al., 2020). Further linear interpolation on some of our data variables assumed an oversimplified assumption of linearity on our data, which introduced spatial bias and reduce data accuracy, hence inherently reduce our models' efficiency.

Regarding machine learning algorithms, notably, some models, including the Transformer and ConvLSTM, displayed sensitivity to data distributions, impacting their consistent performance across diverse datasets. While our U-Net model showcased impressive accuracy, closer inspection revealed its shortcomings in capturing the finer details, especially within intricate upwelling regions. This discrepancy emphasizes the inherent challenge of relying solely on high-level accuracy metrics without considering granular details. Furthermore, deep learning's "black-box" nature (Castelvecchi, 2016) necessitated tools like LIME for model interpretation. However, such tools only offer localized insights, leaving a comprehensive understanding of the decision-making process elusive (Ribeiro et al., 2016). Another constraint was the specificity of our datasets; the observed performance metrics may exhibit biases, suggesting a need for evaluation against a broader set of datasets to ensure model robustness. Crucially, computational constraints, particularly limited RAM, impinged on

our explorations. This limitation was keenly felt with resource-intensive models like U-Net. With more RAM at our disposal, there’s a strong potential to further enhance the model complexity and fine-tuning, possibly achieving greater granularity in predictions and capturing intricate upwelling nuances.

7 Conclusion

Throughout this investigation, our foray into utilizing advanced deep learning architectures to detect upwelling phenomena has culminated in notable findings and insights. From the intricacies of the EfficientNet model to the exploration of Transformer and ConvLSTM’s sensitivities, our methods have cast light on both the potentials and pitfalls of harnessing neural networks in marine research. Our results, especially those drawn from the state-of-art architectures, underscore the critical balance between achieving high-level accuracy and capturing detailed nuances. The challenges of model interpretability, emphasized by our utilization of the LIME framework, reflect the broader issue faced by many in the machine learning community.

Moreover, with our Zarr database, we’ve laid down an initial framework that we believe can be valuable for future marine research endeavors. By offering a variety of variables, we hope to provide a more comprehensive view of marine phenomena for fellow researchers, motivating new research into other variables from the standard sea surface temperature. Central to our work is the meticulous exploration of methods and their outcomes, leading us to a refined understanding of upwelling events and the analytical tools at our disposal. As the field of computational marine research continues to expand, we anticipate that our groundwork here will be a stepping stone towards fresh approaches and deeper insights.

References

- Achanta, R., Shaji, A., Smith, K., Lucchi, A., Fua, P., & Süsstrunk, S. (2012). SLIC superpixels compared to state-of-the-art superpixel methods. *IEEE Transactions on Pattern Analysis and Machine Intelligence*, 34(11), 2274–2282. <https://doi.org/10.1109/TPAMI.2012.120>
- Alvarez, I., Gomez-Gesteira, M., deCastro, M., Gomez-Gesteira, J., & Dias, J. (2010). Summer upwelling frequency along the western cantabrian coast from 1967 to 2007. *Journal of Marine Systems*, 79(1), 218–226. <https://doi.org/10.1016/j.jmarsys.2009.09.004>
- Awo, F. M., Rouault, M., Ostrowski, M., Tomety, F. S., Da-Allada, C. Y., & Jouanno, J. (2022). Seasonal cycle of sea surface salinity in the angola upwelling system. *Journal of Geophysical Research: Oceans*, 127(7), e2022JC018518. <https://doi.org/10.1029/2022JC018518>

- Bakun, A. (1990). Global climate change and intensification of coastal ocean upwelling. *Science (New York, N.Y.)*, 247(4939), 198–201. <https://doi.org/10.1126/science.247.4939.198>
- Becker, J. J., Sandwell, D. T., Smith, W. H. F., Braud, J., Binder, B., Depner, J., Fabre, D., Factor, J., Ingalls, S., Kim, S.-H., Ladner, R., Marks, K., Nelson, S., Pharaoh, A., Trimmer, R., Von Rosenberg, J., Wallace, G., & Weatherall, P. (2009). Global bathymetry and elevation data at 30 arc seconds resolution: SRTM30_plus. *Marine Geodesy*, 32(4), 355–371. <https://doi.org/10.1080/01490410903297766>
- Benazzouz, A., Mordane, S., Orbi, A., Chagdali, M., Hilmi, K., Atillah, A., Lluís Pelegrí, J., & Hervé, D. (2014). An improved coastal upwelling index from sea surface temperature using satellite-based approach – the case of the canary current upwelling system. *Continental Shelf Research*, 34, 38–54. <https://doi.org/10.1016/j.csr.2014.03.012>
- Bessa, I., Makaoui, A., Agouzouk, A., Idrissi, M., Hilmi, K., & Afifi, M. (2019). Seasonal variability of the ocean mixed layer depth depending on the cape ghir filament and the upwelling in the moroccan atlantic coast. *Materials Today: Proceedings*, 13, 637–645. <https://doi.org/10.1016/j.matpr.2019.04.023>
- Bresenham, J. E. (1965). Algorithm for computer control of a digital plotter. *IBM Systems Journal*, 4(1), 25–30. <https://doi.org/10.1147/sj.41.0025>
- Brock, J. C., McClain, C. R., Luther, M. E., & Hay, W. W. (1991). The phytoplankton bloom in the northwestern arabian sea during the southwest monsoon of 1979. *Journal of Geophysical Research: Oceans*, 96, 20623–20642. <https://doi.org/10.1029/91JC01711>
- Castelvecchi, D. (2016). Can we open the black box of AI? *Nature News*, 538(7623), 20. <https://doi.org/10.1038/538020a>
- CF Conventions. (n.d.). Ocean mixed layer thickness defined by sigma theta. In *Ocean_mixed_layer_thickness*
- Cushing, D. (1971). Upwelling and the production of fish. In *Advances in marine biology* (pp. 255–334). Elsevier. [https://doi.org/10.1016/S0065-2881\(08\)60344-2](https://doi.org/10.1016/S0065-2881(08)60344-2)
- Dask Development Team. (2016). *Dask: Library for dynamic task scheduling*. <http://dask.pydata.org>
- Deser, C., Alexander, M. A., Xie, S.-P., & Phillips, A. S. (2010). Sea surface temperature variability: Patterns and mechanisms. *Annual Review of Marine Science*, 2, 115–143. <https://doi.org/10.1146/annurev-marine-120408-151453>
- Ding, H., Alexander, M. A., & Jacox, M. G. (2021). Role of geostrophic currents in future changes of coastal upwelling in the california current system. *Geophysical Research Letters*, 48(3), e2020GL090768. <https://doi.org/10.1029/2020GL090768>
- Dohan, K. (2021). Ocean surface current analyses real-time (OSCAR) surface currents - final 0.25 degree (version 2.0). <https://doi.org/10.5067/OSCAR-25F20>
- European Union-Copernicus Marine Service. (2018). Global ocean physics reanalysis. <https://doi.org/10.48670/MOI-00021>
- European Union-Copernicus Marine Service. (2021). GLOBAL OCEAN GRIDDED 14 SEA SURFACE HEIGHTS AND DERIVED VARIABLES REPROCESSED (1993-ONGOING). <https://doi.org/10.48670/MOI-00148>

- European Union-Copernicus Marine Service. (2022). Global ocean colour (copernicus-GlobColour), bio-geo-chemical, 14 (monthly and interpolated) from satellite observations (1997-ongoing). <https://doi.org/10.48670/MOI-00281>
- Frey, P. W., & Adesman, P. (1976). Recall memory for visually presented chess positions. *Memory & Cognition*, 4(5), 541–547.
- Garvine, R. W. (1973). The effect of bathymetry on the coastal upwelling of homogeneous water. *Journal of Physical Oceanography*, 3(1), 47–56. [https://doi.org/10.1175/1520-0485\(1973\)003<0047:TEOBOT>2.0.CO;2](https://doi.org/10.1175/1520-0485(1973)003<0047:TEOBOT>2.0.CO;2)
- Gobet, F., & Lane, P. C. R. (2012). Chunking mechanisms and learning. In N. M. Seel (Ed.), *Encyclopedia of the sciences of learning* (pp. 541–544). Springer US. https://doi.org/10.1007/978-1-4419-1428-6_1731
- Hammond, M. L., Jebri, F., Srokosz, M., & Popova, E. (2022). Automated detection of coastal upwelling in the western indian ocean: Towards an operational “upwelling watch” system. *Frontiers in Marine Science*, 9, 950733. <https://doi.org/10.3389/fmars.2022.950733>
- Harris, C. R., Millman, K. J., Van Der Walt, S. J., Gommers, R., Virtanen, P., Cournapeau, D., Wieser, E., Taylor, J., Berg, S., Smith, N. J., Kern, R., Picus, M., Hoyer, S., Van Kerkwijk, M. H., Brett, M., Haldane, A., Del Río, J. F., Wiebe, M., Peterson, P., ... Oliphant, T. E. (2020). Array programming with NumPy. *Nature*, 585(7825), 357–362. <https://doi.org/10.1038/s41586-020-2649-2>
- Hersbach, H., Bell, B., Berrisford, P., Hirahara, S., Horányi, A., Muñoz-Sabater, J., Nicolas, J., Peubey, C., Radu, R., Schepers, D., Simmons, A., Soci, C., Abdalla, S., Abellan, X., Balsamo, G., Bechtold, P., Biavati, G., Bidlot, J., Bonavita, M., ... Thépaut, J.-N. (2020). The ERA5 global reanalysis. *Quarterly Journal of the Royal Meteorological Society*, 146(730), 1999–2049. <https://doi.org/10.1002/qj.3803>
- Hoyer, S., Roos, M., Joseph, H., Magin, J., Cherian, D., Fitzgerald, C., Hauser, M., Fujii, K., Maussion, F., Imperiale, G., Clark, S., Kleeman, A., Nicholas, T., Kluyver, T., Westling, J., Munroe, J., Amici, A., Barghini, A., Banihirwe, A., ... Wolfram, P. J. (2022, October 13). *Xarray* (Version v2022.10.0). Zenodo. <https://doi.org/10.5281/ZENODO.7195919>
- Izumo, T., Montégut, C. B., Luo, J.-J., Behera, S. K., Masson, S., & Yamagata, T. (2008). The role of the western arabian sea upwelling in indian monsoon rainfall variability. *Journal of Climate*, 21(21), 5603–5623. <https://doi.org/10.1175/2008JCLI2158.1>
- Jean-Michel, L., Eric, G., Romain, B.-B., Gilles, G., Angélique, M., Marie, D., Clément, B., Mathieu, H., Olivier, L. G., Charly, R., Tony, C., Charles-Emmanuel, T., Florent, G., Giovanni, R., Mounir, B., Yann, D., & Pierre-Yves, L. T. (2021). The copernicus global 1/12° oceanic and sea ice GLORYS12 reanalysis. *Frontiers in Earth Science*, 9, 698876. <https://doi.org/10.3389/feart.2021.698876>
- Jebri, F., Srokosz, M., Jacobs, Z. L., Nencioli, F., & Popova, E. (2022). Earth observation and machine learning reveal the dynamics of productive upwelling regimes on the agulhas bank. *Frontiers in Marine Science*, 9, 872515. <https://doi.org/10.3389/fmars.2022.872515>

- Jolliffe, I. T., & Cadima, J. (2016). Principal component analysis: A review and recent developments. *Philosophical Transactions. Series A, Mathematical, Physical, and Engineering Sciences*, 374(2065), 20150202. <https://doi.org/10.1098/rsta.2015.0202>
- Kim, D., Choi, J.-G., Park, J., Kwon, J.-I., Kim, M.-H., & Jo, Y.-H. (2023). Upwelling processes driven by contributions from wind and current in the southwest east sea (japan sea). *Frontiers in Marine Science*, 10, 1165366. <https://doi.org/10.3389/fmars.2023.1165366>
- Krasnopolsky, V. M., Fox-Rabinovitz, M. S., & Chalikov, D. V. (2005). New approach to calculation of atmospheric model physics: Accurate and fast neural network emulation of longwave radiation in a climate model. *Monthly Weather Review*, 133(5), 1370–1383. <https://doi.org/10.1175/MWR2923.1>
- Lahiri, S. P., & Vissa, N. K. (2022). Assessment of indian ocean upwelling changes and its relationship with the indian monsoon. *Global and Planetary Change*, 208, 103729. <https://doi.org/10.1016/j.gloplacha.2021.103729>
- Lentz, S. J., & Chapman, D. C. (2004). The importance of nonlinear cross-shelf momentum flux during wind-driven coastal upwelling*. *Journal of Physical Oceanography*, 34(11), 2444–2457. <https://doi.org/10.1175/JPO2644.1>
- Lill, C. (1978). The influence of bathymetry on coastal upwelling. *University of Wollongong Thesis Collection 1954-2016*. <https://ro.uow.edu.au/theses/2658>
- MacQueen, J. (1967, January 1). Some methods for classification and analysis of multivariate observations. In *Proceedings of the fifth berkeley symposium on mathematical statistics and probability, volume 1: Statistics* (pp. 281–298). University of California Press. Retrieved September 11, 2023, from <https://projecteuclid.org/ebooks/berkeley-symposium-on-mathematical-statistics-and-probability/Proceedings-of-the-Fifth-Berkeley-Symposium-on-Mathematical-Statistics-and/chapter/Some-methods-for-classification-and-analysis-of-multivariate-observations/bsmsp/1200512992>
- Meteorological Conventions [[Online; accessed 2023-09-29]]. (2022).
- Miles, A., Jakirham, Bussonnier, M., Moore, J., Orfanos, D. P., Bourbeau, J., Fulton, A., Lee, G., Zain Patel, Bennett, D., Rocklin, M., AWA BRANDON AWA, Saransh Chopra, Abernathey, R., Kristensen, M. R. B., De Andrade, E. S., Durant, M., Schut, V., Dussin, R., . . . Bolarinwa, E. (2023, June 14). *Zarr-developers/zarr-python: V2.15.0* (Version v2.15.0). Zenodo. <https://doi.org/10.5281/ZENODO.8039103>
- Miller, G. A. (1956). The magical number seven, plus or minus two: Some limits on our capacity for processing information. *Psychological Review*, 63(2), 81–97. <https://doi.org/10.1037/h0043158>
- Mladek, R. (2019, September 24). *How is the ocean mixed layer thickness (mloxst) variable defined?* [European centre for medium-range weather forecasts]. <https://confluence.ecmwf.int/display/S2S/S2S+Ocean+mixed+layer+thickness+defined+by+sigma+theta+0.01+kgm-3>
- Moore, J., Basurto-Lozada, D., Besson, S., Bogovic, J., Bragantini, J., Brown, E. M., Burel, J.-M., Casas Moreno, X., De Medeiros, G., Diel, E. E., Gault, D., Ghosh, S. S., Gold, I., Halchenko, Y. O., Hartley, M., Horsfall, D., Keller, M. S., Kittisopikul, M., Kovacs,

- G., ... Swedlow, J. R. (2023). OME-zarr: A cloud-optimized bioimaging file format with international community support. *Histochemistry and Cell Biology*, 160(3), 223–251. <https://doi.org/10.1007/s00418-023-02209-1>
- NASA Ocean Biology Processing Group. (2015). MODIS-aqua level 2 ocean color data version 2014. https://doi.org/10.5067/AQUA/MODIS_OC.2014.0
- NASA/JPL. (2015). GHRSSST level 4 MUR global foundation sea surface temperature analysis (v4.1). <https://doi.org/10.5067/GHGMR-4FJ04>
- Nigam, T., Pant, V., & Prakash, K. R. (2018). Impact of indian ocean dipole on the coastal upwelling features off the southwest coast of india. *Ocean Dynamics*, 68(6), 663–676. <https://doi.org/10.1007/s10236-018-1152-x>
- Olauson, J. (2018). ERA5: The new champion of wind power modelling? *Renewable Energy*, 126, 322–331. <https://doi.org/10.1016/j.renene.2018.03.056>
- Park, J., Kim, H.-C., Bae, D., & Jo, Y.-H. (2020). Data reconstruction for remotely sensed chlorophyll-a concentration in the ross sea using ensemble-based machine learning. *Remote Sensing*, 12(11), 1898. <https://doi.org/10.3390/rs12111898>
- Picado, A., Vaz, N., Alvarez, I., & Dias, J. M. (2023). Modelling coastal upwelling off NW iberian peninsula: New insights on the fate of phytoplankton blooms. *Science of The Total Environment*, 874, 162416. <https://doi.org/10.1016/j.scitotenv.2023.162416>
- Pitcher, G., Figueiras, F., Hickey, B., & Moita, M. (2010). The physical oceanography of upwelling systems and the development of harmful algal blooms. *Progress in oceanography*, 55(1), 5–32. <https://doi.org/10.1016/j.pocean.2010.02.002>
- Pollack, N. (2023, March 14). *Zarr format - ESDIS standards coordination office - earthdata wiki* [EarthData wiki]. Retrieved September 29, 2023, from <https://wiki.earthdata.nasa.gov/display/ESO/Zarr+Format>
- Rao, A. D., Joshi, M., & Ravichandran, M. (2008). Oceanic upwelling and downwelling processes in waters off the west coast of india. *Ocean Dynamics*, 58(3), 213–226. <https://doi.org/10.1007/s10236-008-0147-4>
- Ray, S., Swain, D., Ali, M. M., & Bourassa, M. A. (2022). Coastal upwelling in the western bay of bengal: Role of local and remote windstress. *Remote Sensing*, 14(19), 4703. <https://doi.org/10.3390/rs14194703>
- Reynolds, R. W., Rayner, N. A., Smith, T. M., Stokes, D. C., & Wang, W. (2002). An improved in situ and satellite SST analysis for climate. *Journal of Climate*, 15(13), 1609–1625. [https://doi.org/10.1175/1520-0442\(2002\)015<1609:AIISAS>2.0.CO;2](https://doi.org/10.1175/1520-0442(2002)015<1609:AIISAS>2.0.CO;2)
- Ribeiro, M. T., Singh, S., & Guestrin, C. (2016). "why should i trust you?": Explaining the predictions of any classifier. *Proceedings of the 22nd ACM SIGKDD International Conference on Knowledge Discovery and Data Mining*, 1135–1144. <https://doi.org/10.1145/2939672.2939778>
- Ronneberger, O., Fischer, P., & Brox, T. (2015, May 18). U-net: Convolutional networks for biomedical image segmentation. <https://doi.org/10.48550/arXiv.1505.04597>
- Schott, F., Swallow, J. C., & Fieux, M. (1990). The somali current at the equator: Annual cycle of currents and transports in the upper 1000 m and connection to neighbouring

- latitudes. *Deep Sea Research Part A. Oceanographic Research Papers*, 37(12), 1825–1848. [https://doi.org/10.1016/0198-0149\(90\)90080-F](https://doi.org/10.1016/0198-0149(90)90080-F)
- Senf, C. (2022). Seeing the system from above: The use and potential of remote sensing for studying ecosystem dynamics. *Ecosystems*, 25(8), 1719–1737. <https://doi.org/10.1007/s10021-022-00777-2>
- Shi, X., Chen, Z., Wang, H., Yeung, D.-Y., Wong, W.-k., & Woo, W.-c. (2015, September 19). Convolutional LSTM network: A machine learning approach for precipitation nowcasting. <https://doi.org/10.48550/arXiv.1506.04214>
- Skoda, P., & Adam, F. (Eds.). (2020). *Knowledge discovery in big data from astronomy and earth observation: Astrogeoinformatics* [OCLC: on1144737450]. Elsevier.
- Sreenath, A. V., Abhilash, S., Vijaykumar, P., & Mapes, B. E. (2022). West coast india’s rainfall is becoming more convective. *npj Climate and Atmospheric Science*, 5(1), 36. <https://doi.org/10.1038/s41612-022-00258-2>
- Sun, F., Yu, F., Si, G., Wang, J., Xu, A., Pan, J., & Tang, Y. (2022). Characteristics and influencing factors of frontal upwelling in the yellow sea in summer. *Acta Oceanologica Sinica*, 41(7), 84–96. <https://doi.org/10.1007/s13131-021-1967-z>
- Tan, M., & Le, Q. V. (2020a, September 11). EfficientNet: Rethinking model scaling for convolutional neural networks. <https://doi.org/10.48550/arXiv.1905.11946>
- Tan, M., & Le, Q. V. (2020b, September 11). EfficientNet: Rethinking model scaling for convolutional neural networks. <https://doi.org/10.48550/arXiv.1905.11946>
- Trenberth, E., & Shea, J. (1987). On the evolution of the southern oscillation. *Monthly Weather Review*, 3078–3096. [https://doi.org/10.1175/1520-0493\(1987\)115<3078:OTEOTS>2.0.CO;2](https://doi.org/10.1175/1520-0493(1987)115<3078:OTEOTS>2.0.CO;2)
- Umaroh, Anggoro, S., & Muslim. (2017). The dynamics of sea surface height and geostrophic current in the arafura sea. *IOP Conference Series: Earth and Environmental Science*, 55, 012046. <https://doi.org/10.1088/1755-1315/55/1/012046>
- Vance, T. C., Wengren, M., Burger, E., Hernandez, D., Kearns, T., Medina-Lopez, E., Merati, N., O’Brien, K., O’Neil, J., Potemra, J. T., Signell, R. P., & Wilcox, K. (2019). From the oceans to the cloud: Opportunities and challenges for data, models, computation and workflows. *Frontiers in Marine Science*, 6. Retrieved October 1, 2023, from <https://www.frontiersin.org/articles/10.3389/fmars.2019.00211>
- Vaswani, A., Shazeer, N., Parmar, N., Uszkoreit, J., Jones, L., Gomez, A. N., Kaiser, L., & Polosukhin, I. (2023, August 1). Attention is all you need. <https://doi.org/10.48550/arXiv.1706.03762>
- Vinayachandran, P. N., Murty, V. S. N., & Ramesh Babu, V. (2002). Observations of barrier layer formation in the bay of bengal during summer monsoon: BARRIER LAYER IN THE BAY OF BENGAL. *Journal of Geophysical Research: Oceans*, 107, SRF 19–1–SRF 19–9. <https://doi.org/10.1029/2001JC000831>
- Wiggert, J. D., Murtugudde, R. G., & Christian, J. R. (2006). Annual ecosystem variability in the tropical indian ocean: Results of a coupled bio-physical ocean general circulation model. *Deep Sea Research Part II: Topical Studies in Oceanography*, 53(5), 644–676. <https://doi.org/10.1016/j.dsr2.2006.01.027>

- Yu, L. (2003). Variability of the depth of the 20°C isotherm along 6°N in the bay of bengal: Its response to remote and local forcing and its relation to satellite SSH variability. *Deep Sea Research Part II: Topical Studies in Oceanography*, 50(12), 2285–2304. [https://doi.org/10.1016/S0967-0645\(03\)00057-2](https://doi.org/10.1016/S0967-0645(03)00057-2)
- Yu, S., Bai, Y., Xianqiang He, Gong, F., & Li, T. (2022, September 19). A new merged dataset of global ocean chlorophyll-a concentration for better trend detection. <https://doi.org/10.5281/ZENODO.7092219>
- Zhang, X., & Mochizuki, T. (2022). Sea surface height fluctuations relevant to indian summer monsoon over the northwestern indian ocean. *Frontiers in Climate*, 4. Retrieved September 10, 2023, from <https://www.frontiersin.org/articles/10.3389/fclim.2022.1008776>